

Hybrid wave/current energy harvesting with a flexible piezoelectric plate

Kourosh Shoele†

Department of Mechanical Engineering, Joint College of Engineering, Florida A&M University-Florida State University, Tallahassee, FL 32310, USA

(Received 21 January 2022; revised 26 May 2023; accepted 7 July 2023)

We investigate the dynamics and energy production capability of a flexible piezoelectric plate submerged close to the free surface and exposed to incident head gravity waves and current. A theoretical model is derived in which the flag and its wake are represented with a vortex line while the body of the fluid is considered to be inviscid. The model is employed to describe the hydrodynamic interactions between a flexible plate, its wake, gravity incident waves and the current. The model reveals two distinct vibration states of a piezoelectric device corresponding to almost similar optimal energy production levels. The first is associated with the cantilever fluttering mode of the plate, with limited dependency on the plate's flexibility across different Froude numbers and incoming wave frequencies. The other resembles the flow-induced flapping mode in more flexible plates, with the energy output showing a higher dependency on plate flexibility. The concurrent existence of these two energetic modes allows adjustment of the plate length to consistently achieve the maximum energy production level across different flow conditions. The role of the Froude number of the system's responses is explored and correlated to the appearance of gravity wave groups on the surface, each propagating with a different wavenumber. It is shown that a submergence depth of less than half of the body length is required to reach a high energetic condition in subcritical and critical flows. Finally, the optimal inductive and resistive values are related to proper matching between flow, mechanical and electrical time scales.

Key words: flow-structure interactions, vortex dynamics, wave-structure interactions

1. Introduction

The wave energy resource is significant and could supply 10–20% of the world's energy demand (Aderinto & Li 2018). Different technologies have been proposed to extract renewable energy from ocean current and ocean waves (Babarit 2017). Still, few

† Email address for correspondence: kshoele@fsu.edu

technologies can harvest energy from these two resources concurrently. One promising candidate is to use the coupling between fluid and structure in terms of vortex-induced vibration, galloping and fluttering response to either directly enable energy transfer from the incoming current (Zhu & Peng 2009) or actively modify the impedance of the device to capture ocean energy more efficiently (Falnes & Kurniawan 2020; Ringwood 2020). Deployable and flexible structures are good candidates to enhance the performance of energy harvesting devices while addressing the reliability and survivability challenges facing conventional designs based on rigid-body systems (Pecher & Kofoed 2017). The flexible wave energy converters such as the wave carpet (Koola & Ibragimov 2003; Alam 2012) and piezoelectric wave energy converter (Jbaily & Yeung 2015) use the cyclic wave action to generate an alternating current electrical energy. These devices are easily adjustable and can be employed as wave attenuation devices and hybrid wave/current energy harvesters on fixed and moving marine structures. They can also be combined with other devices to enhance the locomotion of marine vehicles (Collins *et al.* 2021).

A flexible thin structure with distributed wave energy converters, analogous to a piezoelectric plate, is a canonical rendition of a wide range of the above multi-segmented flexible energy harvesting concepts (Erturk & Inman 2011). Piezoelectric thin structures are employed to harvest wave energy directly (Viet, Wu & Wang 2017; Mutsuda et al. 2019), or they are used as a model to study the asymptotic response of multi-segmented conventional devices, such as M4 and Pelamis, wherein the energy is captured from differential deformation of adjacent segments (Stansby, Moreno & Stallard 2015; Peng et al. 2020). These systems, in the limit of many interconnecting bodies, resemble the canonical piezoelectric plate with infinitesimal neighbouring electrical circuits in which a simple mathematical model can capture the role of mechanical-to-electrical conversion as well as the resistance capacitance and inductance components of the electrical circuit (Doaré & Michelin 2011; Michelin & Doaré 2013). Another related power harvesting system with similar principles is electro-active polymers (Babarit et al. 2013). All of these technologies have the advantage of transforming the mechanical actuation to electrical output directly, and therefore eliminating the need for including complex mechanical power take-off and power conversion systems (Renzi et al. 2021). The coupled hydro-electro-mechanic response of these structures has been studied near the free surface Renzi (2016), next to the vertical wall (Zheng et al. 2020), and as an array of energy harvesters (Mutsuda et al. 2013). Furthermore, previous research has explored using flexible plates as adjustable floaters and wave energy dissipation devices (Selvan & Behera 2020; Zheng et al. 2021). In particular, the use of floating plates for harvesting wave energy is explored in Michele et al. (2020) and Michele, Zheng & Greaves (2022), wherein a theoretical model based on structural mode shapes of a circular plate is proposed to examine the wave power extraction capacity of these concepts.

In a recent study conducted by Mougel & Michelin (2020), it was discovered that the flapping dynamics of a flexible plate in potential flow is influenced significantly by the presence of the free surface and resonant conditions between the plate and surface gravity waves. Moreover, previous research by Renzi (2016) highlighted that optimal energy harvesting by a piezoelectric plate in a purely harmonic incoming wave relies on constructive matching between the plate's natural frequency and the wave frequency. Building upon these findings, the current study explores how the flow interaction among a flexible piezoelectric plate, its wake, and the free surface can be utilized to manipulate the dynamic characteristics of hybrid wave/current energy harvesters and enhance their energy capturing efficiency.

A closely related problem is a hydrofoil oscillation near the free surface as a passive propulsor or energy harvesting device (Rozhdestvensky & Ryzhov 2003). Grue, Mo & Palm (1988) and Crimi & Statler (1964) conducted a mathematical study on the propulsion of a moving and oscillating foil in close proximity to a free surface under two different scenarios: with incoming waves and without incoming waves. In the absence of incoming waves and a stationary free surface, the study revealed that the momentum transfer between the foil and the flow could result in either positive or negative values, leading to an increase or decrease in the thrust force. However, regardless of the specific scenario, the generation of waves always results in a significant amount of wasted energy. With the presence of surface waves, it was shown that potentially, up to 75 % of the incoming wave energy could be captured and leveraged towards propulsion. Similarly, it has been explored that prescribed deforming fishes near the free surface can benefit from the surface waves to adjust their propulsion (Reece & Siekmann 1964; Fish & Rohr 1999; Shoele & Zhu 2015). It is interesting to study how through proper selection of structural parameters, one can take advantage of the combined effects of current and wave for energy harvesting applications and achieve optimal operating conditions.

This paper employs a mathematical model of a flexible piezoelectric plate placed at a finite depth below the free surface to study the energy harvesting regimes. Wide ranges of incoming wave frequency, submergence depth and current are investigated. The effects of mechanical and electrical parameters on the energy transfer between flow and structure are quantified, and major response modes are examined. Finally, the conclusion and discussion about future directions are presented.

2. Problem formulation

2.1. Configuration

We consider the dynamics of a two-dimensional thin neutrally buoyant flexible plate of length 2b, with b being the half-chord length placed in a uniform axial flow of velocity u and density ρ at a distance H beneath the mean free surface (figure 1). The flow is assumed to be incompressible, inviscid and infinitely deep. The infinite depth assumption is made to simplify the theoretical modelling. In addition, the infinite depth assumption is appropriate for the current problem since, in the anticipated energy harvesting applications, the plate's length is much smaller than the water depth. Here, we assume the clamped boundary condition at the leading edge, and the free boundary condition at the trailing edge of the plate. In addition, it is considered that both surfaces of the plate are covered with infinitesimal piezoelectric patches with segmentation lengths much smaller than b. Each segment is attached to an independent energy harvesting system with linear resistance R, capacitance C, and inductance L elements. The sandwich plate's mass per unit length is m_s , and its equivalent bending stiffness is k_b . Since the plate is very thin, the inertial effect of the plate mass is negligible and therefore is not considered.

2.2. Governing equations

It is assumed that the oscillation amplitudes and the amplitudes of the incoming waves are small. This allows us to use linearized equations of the plate and flow boundary conditions. We denote the vertical deflection of the plate with Y(x, t), and the electric voltage difference between a small piezoelectric patch on the top and bottom surfaces of the flag with V(x, t). The piezoelectric patch is connected to the output circuit with resistance and inductance elements, as shown in figure 1. It is assumed that $Y(x, t) = O(\epsilon_p b) \ll b$ for a

K. Shoele

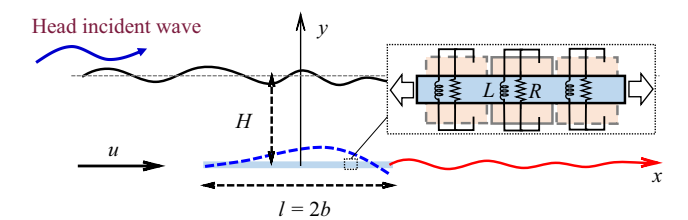


Figure 1. Schematic configuration of a piezoelectric plate beneath the free surface in uniform flow exposed to an incident harmonic wave. In this study, the incident wave is assumed to propagate in the direction of the current, which is also referred to as the head wave (Grue & Palm 1985).

small ϵ_p value. Here, ϵ_p is related to incoming wave amplitude as $\epsilon_p \approx A_0/b$, with A_0 being the incoming wave amplitude. For a thin submerged plate, the structural inertial effects are negligible compared to the bending effect and fluid forces; therefore, the flag is assumed to be massless. Furthermore, it is assumed that the gravity and buoyancy forces cancel each other for the neutrally buoyant flag considered in this study, and the initial configuration of the plate is force-free. The non-dimensional variables shown with $\hat{}$ are defined as

$$\hat{x} = \frac{x}{b}, \quad \hat{Y} = \frac{Y}{b}, \quad \hat{t} = \frac{ut}{b}, \quad \hat{V} = \frac{V}{u\sqrt{\rho b/C}}.$$
 (2.1*a-d*)

Here, the non-dimensionalization is done based on b, b/u, ρ , $u\sqrt{\rho b/C}$ and $u\sqrt{\rho bC}$ as reference length, time, density, voltage and charge density. Henceforth, we adopt the same notation for the non-dimensional variables x, t, Y and V as their dimensional counterparts, for brevity. The non-dimensional linearized electrical-mechanical equations of the piezoelectric plate can be written as (Xia, Michelin & Doaré 2015; Shoele & Mittal 2016)

$$\frac{1}{U^{*2}} \frac{\partial^4 Y}{\partial x^4} - \frac{\alpha}{U^*} \frac{\partial^2 V}{\partial x^2} = -[P], \tag{2.2}$$

$$\beta \frac{\partial^2 V}{\partial t^2} + \frac{\partial V}{\partial t} + \beta \tau^2 V + \frac{\alpha \beta}{U^*} \frac{\partial^4 Y}{\partial x^2 \partial t^2} = 0, \tag{2.3}$$

where U^* is the non-dimensional free-stream velocity, α is the coupling coefficient, β quantifies the resistant property of the electrical circuit, and τ represents the inductance property of the electrical circuit (Thomas, Deü & Ducarne 2009; Xia *et al.* 2015). These characteristic parameters are defined as

$$U^* = ub\sqrt{\frac{\rho b}{k_b}}, \quad \alpha = \frac{\chi}{\sqrt{k_b C}}, \quad \beta = \frac{CuR}{b}, \quad \tau = \frac{b}{u\sqrt{CL}},$$
 (2.4a-d)

where χ is the coupling coefficient of piezoelectric patches, and $[P] = P^+ - P^-$ is the pressure jump across the thin plate. The clamped and free boundary conditions at x = -1 and x = 1 are defined as

$$Y = 0, \quad \frac{\partial Y}{\partial x} = 0 \quad \text{at } x = -1,$$
 (2.5)

$$\frac{1}{U^*} \frac{\partial^2 Y}{\partial x^2} - \alpha V = 0, \quad \frac{1}{U^*} \frac{\partial^3 Y}{\partial x^3} - \alpha \frac{\partial V}{\partial x} = 0 \quad \text{at } x = 1.$$
 (2.6)

As a starting point in describing the flow, we follow the procedure proposed by Crimi & Statler (1964). The flow is assumed to be potential, and the effect of viscosity is confined to

the thin two-dimensional vortex sheet along the plate and the deformable free vortex sheet associated with the wake of the plate. The former part is known as the bounded vortex sheet, and the latter is the free vortex sheet. This model is originally proposed to study the dynamics of thin aerofoils and flexible plates (Thwaites & Meyer 1960; Nitsche & Krasny 1994; Pullin & Wang 2004; Alben 2008b). Moreover, because the plate deflection is of the order of $O(\epsilon)$, the wake is approximately in the y=0 plane. As will be discussed shortly, this model can be used to relate the average flow velocity in the fluid domain to the vortex sheet strength Λ using the Biot–Savart kernel (Saffman 1995). Knowing Λ along the plate, the pressure jump across the plate, [P], can be calculated from the unsteady Bernoulli equation as

$$-\frac{\partial[P]}{\partial x} = \frac{\partial \Lambda}{\partial t} + \frac{\partial \Lambda}{\partial x} \quad \text{at } y = 0.$$
 (2.7)

A potential function $\Phi(x, y, t)$ is used to specify the perturbed flow caused by the presence of the plate, its wake and the incoming waves and current. The velocity potential satisfies the Laplace equation inside the flow region and linearized boundary conditions on the free surface (Haskind 1954; Grue *et al.* 1988; Newman 2018):

$$\nabla^2 \Phi(x, y, t) = 0, \tag{2.8}$$

$$\frac{\partial \eta}{\partial t} + \frac{\partial \eta}{\partial x} = \frac{\partial \Phi}{\partial y}$$
 at $y = h$, (2.9)

$$\frac{\partial \Phi}{\partial t} + \frac{\partial \Phi}{\partial x} = \frac{-1}{Fr^2} \eta \quad \text{at } y = h,$$
 (2.10)

where $\eta(x, t)$ is the height of the free surface disturbance, h = H/b is the normalized submergence depth, and Fr is the Froude number, defined as

$$Fr = \frac{u}{\sqrt{gb}} = \frac{u}{\sqrt{gl/2}},\tag{2.11}$$

with g being the gravitational acceleration. Equation (2.9) is known as the kinematic boundary condition, and (2.10) is known as the dynamic boundary condition of the free surface. The derivations of (2.8)–(2.10) are given in Appendix A.

The velocity potential Φ also satisfies the no-penetration boundary condition on the surface of the piezoelectric plate (Alben 2008*a*,*b*),

$$\frac{\partial Y}{\partial t} + \frac{\partial Y}{\partial x} = \frac{\partial \Phi}{\partial y}$$
 at $y = 0$, (2.12)

and finally, the flow velocity should be finite at the trailing edge. To achieve this, a free vortex is shed from the trailing edge of the plate, and the strength of the newly shed vortex is determined from the Kutta condition at the trailing edge of the piezoelectric plate (Saffman 1995).

Assuming a harmonic incoming wave, we can express Φ as a summation of two harmonic potential functions,

$$\Phi(x, y, t) = \text{Re}[(\phi_0 + \phi_1) e^{i\omega t}],$$
 (2.13)

where Re means the real part of the equation. Here, ϕ_0 and ϕ_1 are functions of spatial coordinates only, where ϕ_0 is the known harmonic potential function of the incident wave with the non-dimensional angular frequency ω , and ϕ_1 is velocity potential due

to disturbed flow as a result of the inclusion of the piezoelectric plate in the flow field. We can further divide ϕ_1 into three components, $\phi_1 = \phi_1^W + \phi_1^I + \phi_1^F$, where ϕ_1^W is the contribution to the potential from the plate and its wake, ϕ_1^I is the contribution from the image system of ϕ_1^W outside the free surface, and ϕ_1^F is the contribution from the free surface when there is no incoming wave. In particular, in order to satisfy the free surface conditions in our problem, the image system consists of a vortex sheet identical to vortex sheets in the plate, and its wake is assumed at h above the free surface. The combined effect of the real vortex sheet and its image ensures that $\phi_1^W + \phi_1^I = 0$ on the mean free surface, therefore ϕ_1^F is the primary function that describes the perturbed free surface.

In this study, we consider only incoming waves propagating in the positive x-direction. These waves are known as the head wave, while if the incident wave propagates opposite to the current direction, then it is known as the following wave (Grue & Palm 1985). The incoming head wave elevation η_0 is expressed as

$$\eta_0 = A_0 \sin\left(\omega t - k_0 x\right),\tag{2.14}$$

where A_0 is the non-dimensional amplitude of the incoming wave, k_0 is the wavenumber of the admissible head wave (Haskind 1954),

$$k_0 = \frac{1}{2Fr^2} [1 + 2\omega Fr^2 - \sqrt{1 + 4\omega Fr^2}], \tag{2.15}$$

and ϕ_0 can be expressed as

$$\phi_0(x, y) = \frac{A_0}{\sqrt{k_0} Fr} e^{k_0(y-h)} e^{-ik_0 x}.$$
 (2.16)

Since the incident wave and consequently the motion of the body are harmonic, the vortex strength along the body and in the wake can be expressed as $\Lambda(x,t) = \text{Re}[\gamma(x)\,\mathrm{e}^{\mathrm{i}\omega t}]$, allowing the non-dimensional ϕ_1^W and ϕ_1^I to be related to $\gamma(x)$ through (Crimi & Statler 1964)

$$\phi_1^W(x, y) = -\frac{1}{2\pi} \int_{-1}^1 \gamma(x') \tan^{-1} \left(\frac{y}{x - x'} \right) dx' - \frac{i\omega \bar{\Gamma}}{2\pi} \int_{1}^{\infty} e^{-i\omega(x' - 1)} \tan^{-1} \left(\frac{y}{x - x'} \right) dx',$$
(2.17)

$$\phi_1^I(x,y) = -\frac{1}{2\pi} \int_{-1}^1 \gamma(x') \tan^{-1} \left(\frac{y-2h}{x-x'} \right) dx' - \frac{i\omega \bar{\Gamma}}{2\pi} \int_{1}^{\infty} e^{-i\omega(x'-1)} \tan^{-1} \left(\frac{y-2h}{x-x'} \right) dx',$$
(2.18)

where $\bar{\Gamma}$ is the harmonic amplitude of total circulation of the plate (i.e. $\Gamma = \text{Re}[\bar{\Gamma} e^{i\omega t}]$), related to γ as

$$\bar{\Gamma} = \int_{-1}^{1} \gamma(x') \, \mathrm{d}x'. \tag{2.19}$$

Finally, $\phi_1^F(x, y)$ can be expressed as

$$\phi_1^F(x,y) = \frac{\mathrm{i}}{2\pi Fr^2} \int_{-1}^1 \gamma(x') G(x';x,y) \, \mathrm{d}x' + \frac{\omega \bar{\Gamma}}{2\pi Fr^2} \int_{1}^{\infty} \mathrm{e}^{-\mathrm{i}\omega(x'-1)} G(x';x,y) \, \mathrm{d}x',$$
(2.20)

where G(x'; x, y) is the fundamental solution for an oscillating point vortex beneath the free surface (Tan 1955, 1957) and is given by

$$G(x'; x, y) = \int_{0}^{\infty} e^{\sigma(y-2h)} \left[\frac{e^{i\sigma(x-x')}}{(\sigma - \sigma_{1})(\sigma - \sigma_{2})} - \frac{e^{-i\sigma(x-x')}}{(\sigma - \sigma_{3})(\sigma - \sigma_{4})} \right] d\sigma$$

$$+ D_{1} \exp\left(\sigma_{1} \left[y - 2h + i(x - x') \right] \right) + D_{2} \exp\left(\sigma_{2} \left[y - 2h + i(x - x') \right] \right)$$

$$+ D_{3} \exp\left(\sigma_{3} \left[y - 2h - i(x - x') \right] \right) + D_{4} \exp\left(\sigma_{4} \left[y - 2h - i(x - x') \right] \right),$$
(2.21)

where

$$\sigma_{1,2} = \frac{1}{2Fr^2} \left[1 - 2\omega Fr^2 \pm \sqrt{1 - 4\omega Fr^2} \right],$$

$$\sigma_{3,4} = \frac{1}{2Fr^2} \left[1 + 2\omega Fr^2 \pm \sqrt{1 + 4\omega Fr^2} \right].$$
(2.22)

Here, σ_1 to σ_4 are the wavenumbers of possible wave trains created as a result of the insertion of the plate, and D_1 to D_4 are complementary coefficients that are calculated such that G(x'; x, y) provides the correct radiation free surface condition at $x \to \pm \infty$. Further information can be found in Reece (1963).

Further information can be found in Reece (1963). The relations of ϕ_1^W , ϕ_1^I and ϕ_1^F to the vortex strength along the body and in the wake γ ((2.17), (2.18) and (2.20)) can be used to express the no-penetration boundary condition (2.12) along the plate ($-1 \le x \le 1$) based on γ as

$$-i\omega \xi(x) - \frac{\partial \xi(x)}{\partial x} + \frac{\partial \phi_0(x, y)}{\partial y} \bigg|_{y=0} = \frac{1}{2\pi} \int_{-1}^1 \frac{\gamma(x')}{x - x'} dx' + \frac{1}{2\pi} \int_{-1}^1 \gamma(x') \left[\frac{x - x'}{(x - x')^2 + (2h)^2} - \frac{i}{Fr^2} G_y(x') \right] dx' - \frac{i\omega \bar{\Gamma}}{2\pi} \int_{1}^{\infty} e^{-i\omega(x'-1)} \left[\frac{1}{x - x'} + \frac{x - x'}{(x - x')^2 + (2h)^2} - \frac{i}{Fr^2} G_y(x') \right] dx', \quad (2.23)$$

where $Y(x, t) = \text{Re}[\xi(x) e^{i\omega t}]$, and $G_y(x') = \partial G(x'; x, y)/\partial y|_{y=0}$. Here, f is used to denote the Cauchy principle value integral. Similarly, other equations can also be written based on the normal modes of time-periodic variables. Using the notation $[P](x, t) = \text{Re}[[p](x) e^{i\omega t}]$ and $V(x, t) = \text{Re}[v(x) e^{i\omega t}]$, (2.2), (2.3) and (2.7) are combined into

$$\left(1 + \frac{\alpha^2 \beta \omega^2}{\beta \omega^2 - i\omega - \beta \tau^2}\right) \frac{\partial^4 \xi}{\partial x^4} = -U^{*2}[p],$$
(2.24)

$$i\omega\gamma + \frac{\partial\gamma}{\partial x} = -\frac{\partial[p]}{\partial x},$$
 (2.25)

with the boundary conditions

$$\xi = \frac{\partial \xi}{\partial x} = 0 \quad \text{at } x = -1, \tag{2.26}$$

$$\frac{\partial^2 \xi}{\partial x^2} = \frac{\partial^3 \xi}{\partial x^3} = 0 \quad \text{at } x = 1,$$
 (2.27)

finite velocity (Kutta condition) at
$$x = 1$$
. (2.28)

The system (2.23)–(2.25) along with boundary conditions (2.26)–(2.28) is solved for ξ , [p] and γ . The electrical power output from the piezoelectric plate is

$$\overline{\dot{W}_e} = \frac{1}{\beta} \frac{\omega}{2\pi} \int_0^{2\pi/\omega} \int_{-1}^1 V^2(x, t) \, \mathrm{d}x \, \mathrm{d}t = \frac{1}{2\beta} \int_{-1}^1 |v(x)|^2 \, \mathrm{d}x. \tag{2.29}$$

The non-dimensional power input from the incoming wave is calculated from (2.30) for the wave train progressing in the direction of u, commonly referred to as the 'head wave':

$$\overline{\dot{W}_w} = E_w \left| c_g + 1 \right|. \tag{2.30}$$

In this relation, $E_w = \frac{1}{2}A_0^2/Fr^2$ is the incoming wave energy density, and $c_g = 1/(2\sqrt{k_0}\,Fr)$ is the group velocity of the head wave. In addition, the mean thrust force acting on the piezoelectric plate, \bar{T} , can be computed from

$$\bar{T} = \bar{T}_p + \bar{S},\tag{2.31}$$

where \bar{T}_p is the thrust force due to the pressure difference along the plate, given by

$$\bar{T}_p = \frac{\omega}{2\pi} \int_0^{2\pi/\omega} \int_{-1}^1 [P](x,t) \, \frac{\partial Y}{\partial x}(x,t) \, \mathrm{d}x \, \mathrm{d}t = \frac{1}{2} \int_{-1}^1 [p](x) \, \xi^*(x) \, \mathrm{d}x. \tag{2.32}$$

Here, ξ^* is the complex conjugate of ξ , and \bar{S} is a non-dimensional suction force at the sharp leading edge of the plate, pointing in the minus x-direction. The suction force is calculated by applying the Blasius formula to a small circle R_{δ_0} of radius δ_0 surrounding the leading edge. In particular, we can write $S = \frac{1}{2} \oint_{R_{\delta_0}} \Psi'^2(z) \, dz$, where z = x + iy is the complex number representing position in the x-y plane, and $\Psi'(z) = u - iv$ is the complex velocity (Saffman 1995).

The mean energy equation, averaged in time, in its non-dimensional form can be expressed as

$$\overline{\dot{W}_w} = \overline{\dot{W}_e} + \overline{T} + \overline{E},\tag{2.33}$$

where \bar{E} is the summation of mean wasted energy from the wake of the plate and scattering surface waves from the inclusion of the plate below the free surface. To quantify the overall efficiency of the piezoelectric plate, we define the energy harvesting efficiency η_P :

$$\eta_P = \frac{\dot{W}_e}{\dot{W}_w}.\tag{2.34}$$

2.3. Numerical method

For the numerical simulation, m+1 Chebyshev–Lobatto collocation points are chosen to discretize $\frac{\partial^2 \xi}{\partial x^2}$ along the plate:

$$x_j = -\cos\left(\frac{j\pi}{m}\right), \quad \text{with } j = 0, \dots, m.$$
 (2.35)

Knowing [p] at the jth collocation point, $\partial^2 \xi / \partial x^2$ can be computed easily from (2.24) along with the boundary conditions at the free end of the plate (2.27). Then, by integrating $\partial^2 \xi / \partial x^2$ twice and incorporating the boundary conditions at the fixed end ((2.27) and

(2.26)), the plate deflection $\xi(x_j)$ can be computed. To solve (2.23), we employ a Glauert series solution for γ ,

$$\gamma(\theta) = 2 \left[a_0 \cot \frac{\theta}{2} + \sum_{j=1}^{\infty} a_j \sin(j\theta) \right], \qquad (2.36)$$

with $\theta = -\arccos(x)$, and rewrite (2.36) as

$$\frac{1}{2\pi} \int_{-1}^{1} \frac{\gamma(x')}{x - x'} \, \mathrm{d}x' = \left[a_0 - \sum_{j=1}^{\infty} a_j \cos(j\theta) \right]. \tag{2.37}$$

We employ Fourier cosine series representations of variables, and group the coefficients of $\cos(j\theta)$ terms to obtain an infinite set of equations to solve for the coefficients. In particular, the governing equation for γ (2.23) can be written as the set of algebraic equations for a_i :

$$a_i - \sum_{i=0}^{\infty} Q_{ij} a_j = r_i,$$
 (2.38)

where Q_{ij} coefficients account for the second and third terms in the right-hand side of (2.23) as highlighted in Crimi & Statler (1964). In (2.38), r_i is obtained from the cosine Fourier expansion coefficients of the left-hand side of (2.23) and can be computed from

$$r_i = [C^{-1}]_{ik} LHS(x_k),$$
 (2.39)

where LHS(x_k) is the summation of all terms on the left-hand side of (2.23) at the collocation point x_k along the plate. The transformation matrix C_{ij} is defined as

$$C_{ij} = \begin{cases} 1, & \text{if } j = 0, \\ -\cos\left(\frac{ij\pi}{m}\right), & \text{if } j \ge 1. \end{cases}$$
 (2.40)

Similarly, upon inserting (2.36) in (2.25), the pressure distribution on the plate can be expressed as

$$[p] = -2 \left[a_0 \cot \frac{\theta}{2} + \sum_{j=1}^{\infty} b_j \sin(j\theta) \right], \qquad (2.41)$$

where

$$b_{j} = \begin{cases} a_{1} + i\omega \left[3a_{0} + a_{1} + \frac{a_{2}}{2} \right], & \text{if } j = 1, \\ a_{j} + \frac{i\omega}{2j} \left[a_{j+1} - a_{j-1} + 2(2a_{0} + a_{1})(-1)^{j+1} \right], & \text{if } j \geq 2. \end{cases}$$

$$(2.42)$$

It appears from (2.41) that [p] is singular at the leading edge x = -1, therefore from (2.24), $\partial^4 \xi / \partial x^4$ is singular at the leading edge. This does not pose a problem as (2.24) is evaluated only for the internal nodes. In particular, we solve the second-order equation (2.24) for ξ_{xx} , and replace the equations on the boundary nodes of x_0 and x_m with the

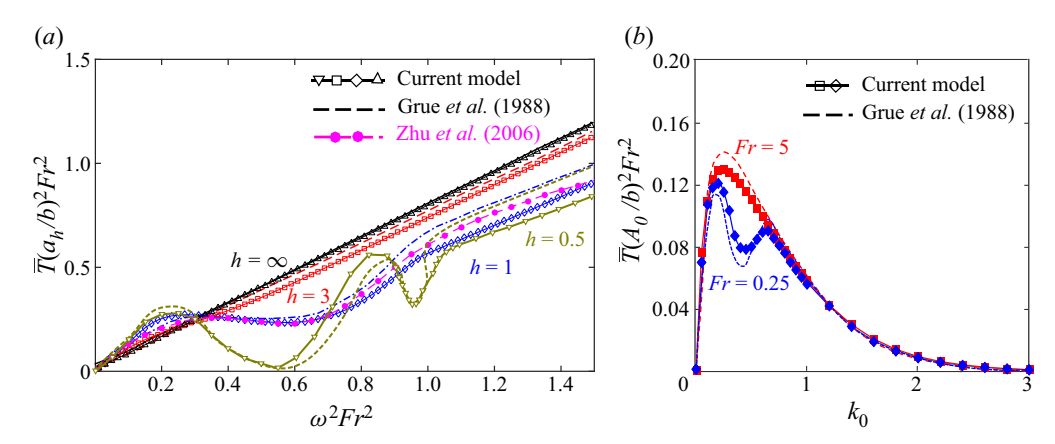


Figure 2. (a) Dependence of thrust force on the heaving frequency of a horizontal plate below the free surface, for Fr = 0.25 and $h = 0.5, 1, 3, \infty$. Dashed lines are for Grue *et al.* (1988); magenta circular symbols are the numerical prediction for Zhu, Liu & Yue (2006) obtained for $a_h/b = 0.05$, with a_h being the heaving amplitude. The other symbols are for the current model. (b) Comparison of the thrust force for different incident wavenumbers between the current model (symbols) and Grue *et al.* (1988) (dashed lines) for a fixed plate with h = 1 and Fr = 0.25 and 5. Here, A_0 and k_0 are the non-dimensional amplitude and wavenumber of the incident wave.

two boundary conditions at the free end of the plate, $\xi_{xx}(x_m) = \xi_{xxx}(x_m) = 0$, to solve the following system of m+1 equations:

$$\left(1 + \frac{\alpha^2 \beta \omega^2}{\beta \omega^2 - i\omega - \beta \tau^2}\right) D_{xx} \xi_{xx} = -U^{*2}[p], \quad \text{for } j = 1, \dots, m - 1, \tag{2.43}$$

$$\xi_{xx}(x_m) = 0, \tag{2.44}$$

$$D_x \, \xi_{xx}(x_m) = 0, \tag{2.45}$$

where D_x and D_{xx} are the first- and second-order Chebyshev differentiation matrices. Following the convergence study, 21 Chebyshev–Lobatto nodes along the plate length are found to be sufficient to discretize the governing equations. Similarly, the series expansions in (2.36) and (2.41) are also truncated to contain only the first 21 terms.

3. Validation

To validate the present model, we compare the thrust force of the plate with Grue *et al.* (1988) for the scenarios in which the plate undergoes periodic heaving motion close to the calm free surface without any incident wave in figure 2(a). Four submergence depths, $h = 0.5, 1, 3, \infty$, are tested, while the Froude number is fixed at Fr = 0.25 for all cases. The non-dimensional amplitude of heaving motion is denoted a_h/b . In addition, the numerical results of the same problem for a three-dimensional foil beneath the free surface by Zhu *et al.* (2006) are also included. In Zhu *et al.* (2006), the heaving motion of a thin NACA0005 foil, with a large span-to-chord length ratio 10 and a small heaving amplitude $a_h/b = 0.05$, is simulated for the submergence depth h = 1. The large span-to-chord ratio of this numerical result creates a practically two-dimensional flow field similar to the conditions examined here. The present result compares well with previous analytical and numerical results. The maximum difference for h < 1 cases is less than 3%, while the maximum difference of 15% is seen between our prediction and reported values in Grue *et al.* (1988) for high frequency and small h = 0.5 cases.

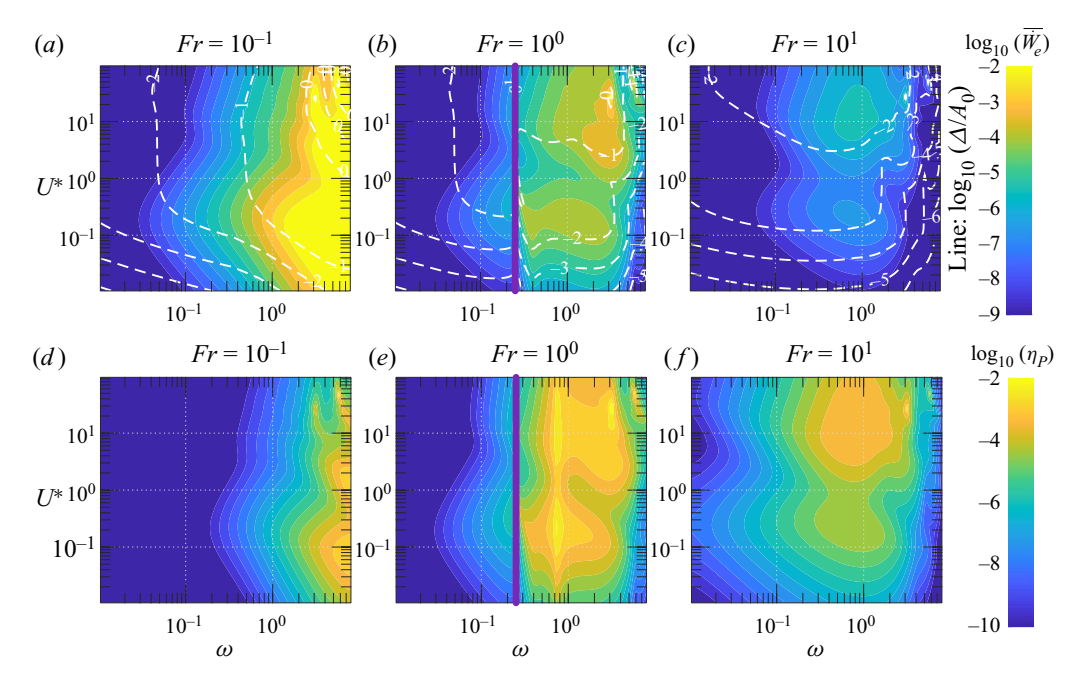


Figure 3. (a-c) The average electrical power output and lateral deflection amplitude (lines), and (b-d) energy efficiency versus ω and U^* for three representative values: Fr=0.1,1,10. Other parameters are fixed at $\alpha=0.5,\beta=1,\tau=0$ and h=1.0. The regions close to ω $Fr^2=\frac{1}{4}$ are marked with a purple line since the proposed linear solution is not valid due to abrupt changes of surface wave propagation modes (Palm & Grue 1999).

In addition, we cross-compare our predictions with the reported values of a fixed plate exposed to the incident waves, as shown in figure 2(b). Here, the plate is kept fixed at its initial position, and the thrust forces for different incoming wavenumbers are compared to reported values in Grue *et al.* (1988). The submergence depth is h = 1, and Fr = 0.25, 5 are tested. The prediction from the current method follows closely the previously reported values, with maximum error less than 10%.

4. Results

In the following, we investigate how the characteristic parameters influence the vibration behaviour and energy harvesting capabilities of the piezoelectric plate energy harvester.

4.1. Effects of reduced velocity

The bending rigidity of a piezoelectric plate is characterized using the non-dimensional reduced velocity U^* presented in (2.4a-d). In figures 3(a-c), the electrical power output $\overline{\dot{W}_e}$ and the ratio of maximum lateral deflection of the plate to the incident wave amplitude Δ/A_0 are plotted for a wide range of $10^{-2} < U^* < 10^2$ and $10^{-2} < \omega < 10$ for three representative Froude numbers: Fr = 0.1 (subcritical flow), Fr = 1 (critical flow), and Fr = 10 (supercritical flow). Here, Δ is defined as the peak-to-peak lateral deflection of the plate, defined as $\Delta = y_{max} - y_{min}$, where $= y_{max}$ and y_{min} are the maximum and minimum lateral positions of the plate. The immediate regions of $\omega Fr^2 = \frac{1}{4}$ are removed from the plots with the purple line. At this condition, the radiative waves originating from the plate

switch from σ_1 to σ_4 waves to include only σ_3 and σ_4 waves, hence the proposed linear solution stops being valid (Palm & Grue 1999). All other parameters are fixed at their representative values h = 1.0, $\alpha = 0.5$, $\beta = 1$ and $\tau = 0$.

For the subcritical flow, the output energy is impacted mainly by the wave frequency, and changes only marginally with the flexibility of the plate, represented by U^* . Nonetheless, for higher frequencies, two distinct maxima are observed for all Fr cases: one at $U^* > 1$ resembling the flow-induced flapping mode of the plate, and the other at $U^* < 1$ related to the cantilever resonance mode of the plate, hereafter referred to as the fluttering mode. Looking at subcritical flow with Fr = 0.1 in figure 3(a), we can see that while \overline{W}_e decays quickly as ω decreases below 1, the maximum deflection of the plate is almost independent of U^* in this range if the plate vibrates with the flapping mode. On the other hand, contour lines with similar Δ/A_0 have a linear trend in the $\log_{10}(\omega) - \log_{10}(U^*)$ plane if the plate oscillates in its fluttering mode. The exception is an isolated small region at higher U^* and $\omega \approx 2$ where there is a sudden increase in the flapping amplitude and the electrical energy output. The same observation can be made across different Fr numbers, wherein the maximum harvested energy is localized at a narrow range of frequencies and U^* . In this condition, the convective time scale of the problem and the encountered wave frequency takes a particular ratio that promotes better energy transfer from the flow to the plate.

The energy harvesting efficiencies η_P , for Fr=0.1,1,10, are shown in figures 3(d-f). The energy harvesting efficiency increases with ω when Fr is small and the flow is critical or subcritical. When $\omega Fr^2 < \frac{1}{4}$, the energy harvesting efficiency shows larger sensitivity to ω compared to U^* . On the other hand, when $\omega Fr^2 > \frac{1}{4}$ (the right-hand side of the purple line of Fr=1 cases, and the entire region of Fr=10 cases in figure 3b), η_P is affected by both U^* and ω . In this case, only one new surface wave σ_2 will be generated in addition to the incident head wave σ_4 , and both of these waves propagate downstream. The incoming wave transmits partially to the electrical energy, while the rest of the energy propagates in the downstream direction as new types of waves.

Figure 4(a) shows the locations of the two highest values of η_P in the ω -U* plane for different Fr numbers. The first branch is located at high $U^* > 1$ values, and the second branch is observed at $U^* < 1$. The highest achievable η_P is always observed for higher Fr cases, while its magnitude along both branches remains close. The position of the optimal case in the first branch follows a power law with exponent ≈ -0.52 , and shifts to lower U^* and higher ω regimes with the decrease of Fr. The changes along the second branch are less dependent on U^* , with power-law exponent -0.27. The plate undergoes different modes of vibration along each of these branches. The plate exhibits a classical travel wave deflection pattern reminiscent of the flag flapping problem along the first branch. Yet the plate vibrates at much smaller U^* compared to that associated with the fluttering instability of light flags (Alben 2008a). In this case, with an increase of Fr, the place of maximum lateral deflection is relocated along the length while the vibration amplitude reduces (figure 4b). On the other hand, the optimal cases along the other branch consistently vibrate in their fluttering modes, as shown in figure 4(c). In this case, the interaction between the first natural frequency of the immersed plate and the frequency of the propagating surface wave increases the oscillation amplitude, and consequently results in a higher level of harvested energy.

The results suggest that one can practically change the plate length to attain maximum energy harvesting efficiency in two distinct response modes, flapping and cantilever fluttering modes. In particular, from the definitions of non-dimensional parameters, we

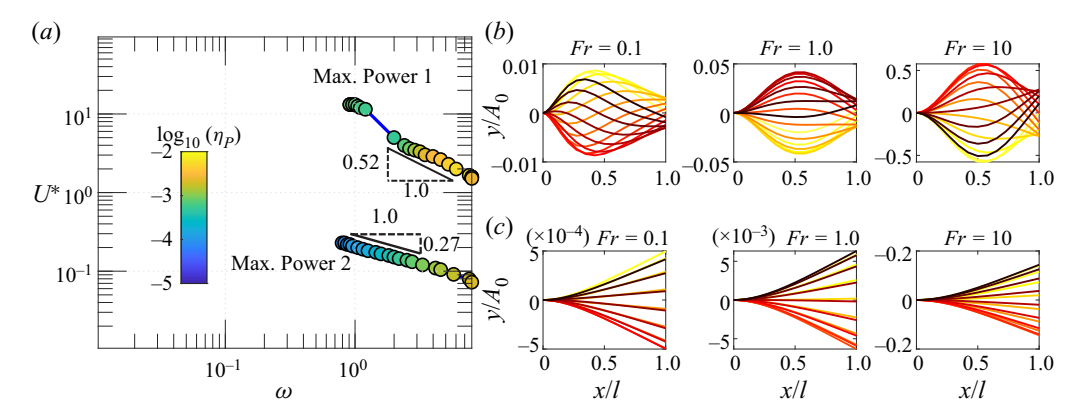


Figure 4. (a) The locations of the most energy efficient conditions in $\omega - U^*$ parametric space with the changes of Fr. (b) Snapshot of the plate deflection over one cycle along the first branch (flapping case), with time instances marked from light to dark colour for a unit incoming wave amplitude. (c) Mode of flutter along the second branch.

can show that $U^* \propto b^{3/2}$, $\omega \propto b^{-1}$ and $Fr \propto b^{-1/2}$, and therefore depending on the flow speed and structural parameters, the plate length can be controlled to place the system on the first optimal branch. Otherwise, the system can also be switched to the cantilever model to maintain maximum energy harvesting efficiency. Also, when the incoming wave spectrum is broadband, the cantilever fluttering mode will continue delivering maximum attainable energy. On the other hand, to benefit from the flapping mode, it is necessary to perform a complex control of U^* , perhaps by adjusting the flow velocity or, equivalently, the advancement speed of the plate.

4.2. Effects of Froude number

The interaction of the surface wave and the submerged plate is highly dependent on the Froude number Fr. Figure 5 compares $\overline{\dot{W}_e}$ and Δ/A_0 as functions of Fr and ω for three representative reduced velocities, 0.1, 1 and 10, selected from the results discussed in the previous subsection. All other parameters are fixed at their representative values $\alpha=0.5$, $\beta=1$, $\tau=0$ and h=1. For the stiff plate (figure 5a), below the critical line of ω $Fr^2=\frac{1}{4}$, the harvested energy is mainly a function of ω , while for the cases above the critical line, the harvested energy is primarily a function of Fr. In this case, the plate is actuated in its cantilever fluttering mode. Vibration amplitude follows a trend similar to that of $\overline{\dot{W}_e}$. At $U^*=1$, the vibration mode starts switching from fluttering to flapping, and the region with higher $\overline{\dot{W}_e}$ extends to lower ω and higher Fr cases (figure 5b).

For the very flexible plate with $U^*=10$ shown in figure 5(c), both \dot{W}_e and Δ/A_0 are predominantly functions of ω , and Fr dependency is observed only over a narrow region in the parametric space. In this case, the energy-producing region shrinks along the ω axis but occurs over a wider range of Fr values. The vibration mode comprises travelling flapping modes with one, two or three nodes along the plate length.

The variations of η_P with ω and Fr are shown in figure 5(d-f). For lower U^* cases, different from \overline{W}_e , the region with large energy harvesting efficiency η_P extends to higher Fr ranges where the plate converts a higher percentage of the incoming wave to electrical energy.

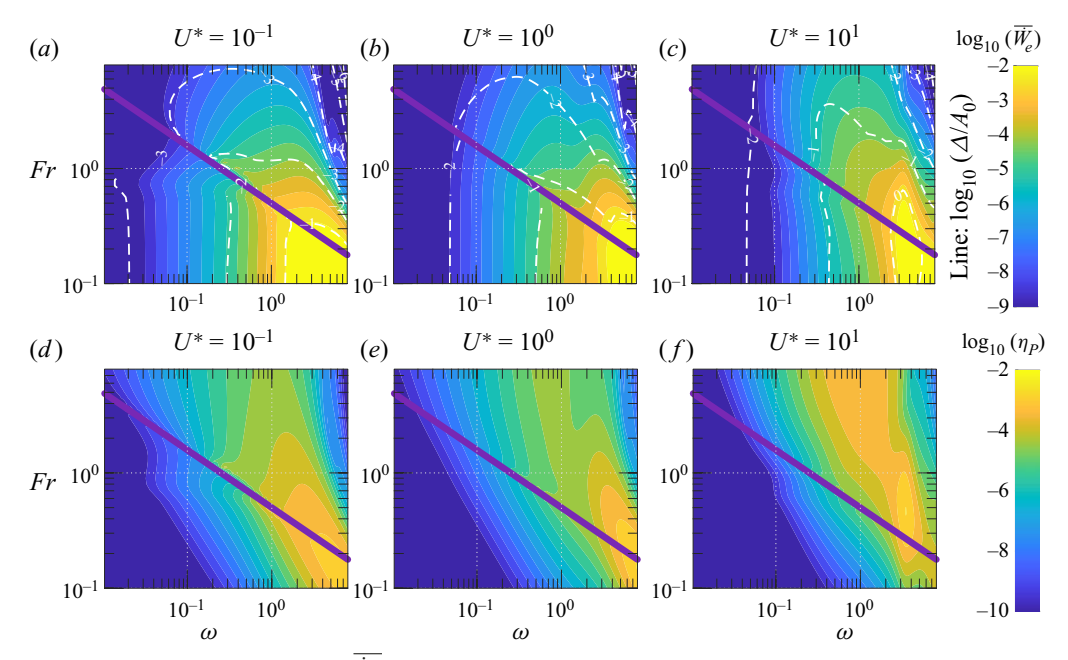


Figure 5. Dependency of (a-c) \dot{W}_e and Δ/A_0 , and (d-f) η_P , versus ω and F for three representative U^* values, 0.1, 1, 10. Other parameters are fixed at $\alpha=0.5$, $\beta=1$, $\tau=0$ and h=1.

A good correlation is identified between the amplitude of vibration and η_P . It is observed that the highest efficiency in these cases is related directly to the amplitude of the fluttering mode, and the highest efficiency could be found over a range of ω just before the dominant vibration mode switching from flapping to fluttering mode. This trend changes at larger reduced velocities, where the highest efficiency is concentrated at a narrow band of ω . The region with high η_P and $\overline{\dot{W}_e}$ coincides at $\omega \approx 3$, with much lower dependency on Fr. It is found that for flexible plates, the wave cannot actuate the first fluttering mode due to a large mismatch between the natural frequencies of the plate and the incoming wave, and instead triggers and amplifies the flapping response of the plate. As a result, the plate harvests simultaneously the energy from the wave and current, and reaches much higher η_P .

4.3. Effects of submergence depth

The plate's submergence depth changes its receptivity to the waves. Figure 6 shows the dependency of \overline{W}_e and Δ with the submergence depth and the wave frequency for subcritical, critical and supercritical conditions. Other parameters are fixed at their reference values. For subcritical conditions, the results are almost independent of the submergence depth if h < 2, equivalently when the submergence of the plate is less than its length. The same behaviour is observed for all U^* cases. The deviation is only for minimal submergence depth where the region with high \overline{W}_e extends to lower ω ranges. In contrast, a larger dependency on the submergence depth can be found for critical and supercritical flows. For these cases, the power output shows a higher decay with depth for less flexible plates than more flexible ones. This is due to a change in the energy harvesting mechanism from wave-induced fluttering motion in stiff plates to wave-triggering flapping motion in

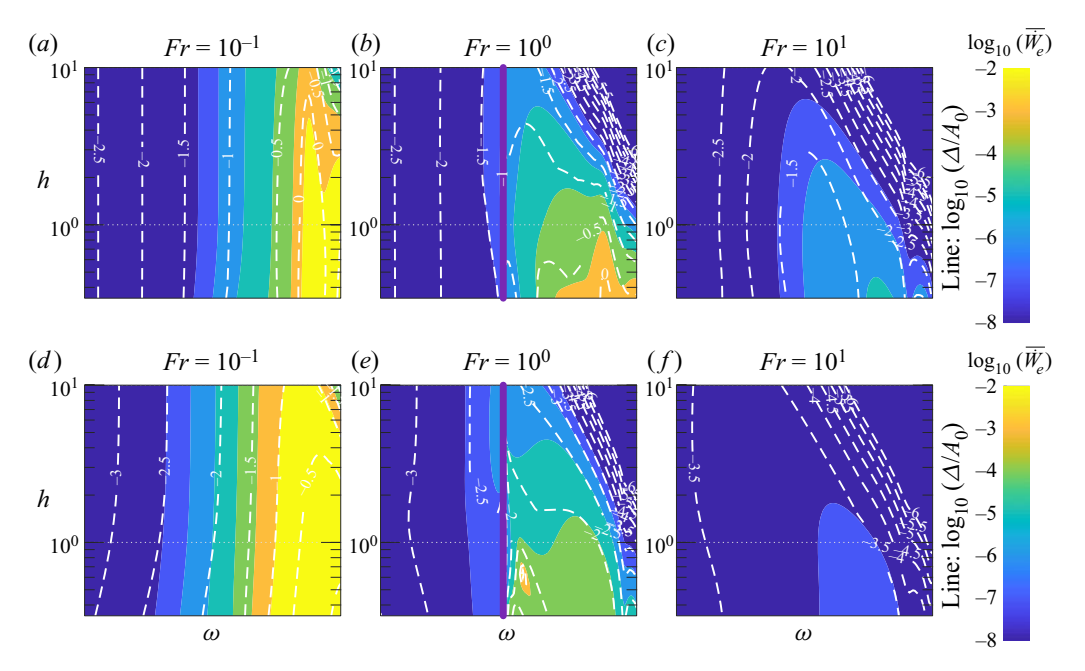


Figure 6. Dependency of the average electrical power output and maximum plate deflection on the submergence depth h for different incoming wave frequencies ω and selected Fr: (a-c) $U^* = 0.1$, and (d-f) $U^* = 10$. The electrical parameters are fixed at the base values $\alpha = 0.5$, $\beta = 1$, $\tau = 0$.

flexible plates. A flexible plate with flapping motion has a larger oscillation amplitude, and as a result, the combination of wave actuation and flow-induced flapping results in a higher amount of harvested energy, despite the wave energy itself decaying with submergence depth. Yet the benefit of the flapping motion declines quickly with an increase of Fr, as the available wave energy weakens very fast with the depth.

The results suggest that the flapping mode reaches the highest energy production if the plate is placed at h < 1 (half of the plate's length) in subcritical and critical conditions. The energy extraction efficiency plots depicted in figure 7 demonstrate that the highest energy efficiency throughout the depth occurs when the system operates under near-critical conditions and exhibits flapping mode vibration. The maximum attainable η_P is smaller for stiffer plates, and concentrates near the free surface for higher Fr conditions. In practice, these optimal conditions can be achieved with longer plates or faster incoming flow; in both cases, it is beneficial to place the plate near the free surface.

4.4. Impact of electrical parameters

The coupling between a piezoelectric plate and a resonant circuit could substantially affect the energy harvesting performance of the piezoelectric flag Xia et al. (2015). These effects are related to α , the coupling coefficient, as well as β and τ , the resistive and inductive properties of the electrical circuit. Figure 8 shows how electrical power output and the maximum plate deflection change with ω across a wide range of the electromechanical coupling parameter α . The other values are fixed at their nominal values. While $\alpha < 0.5$ is expected in conventional piezoelectric materials, higher values can be achieved in multi-segmented systems such as M4 and Pelamis with conventional mechanical energy capturing derives. It is found that electrical power output is affected mainly by the wave

K. Shoele

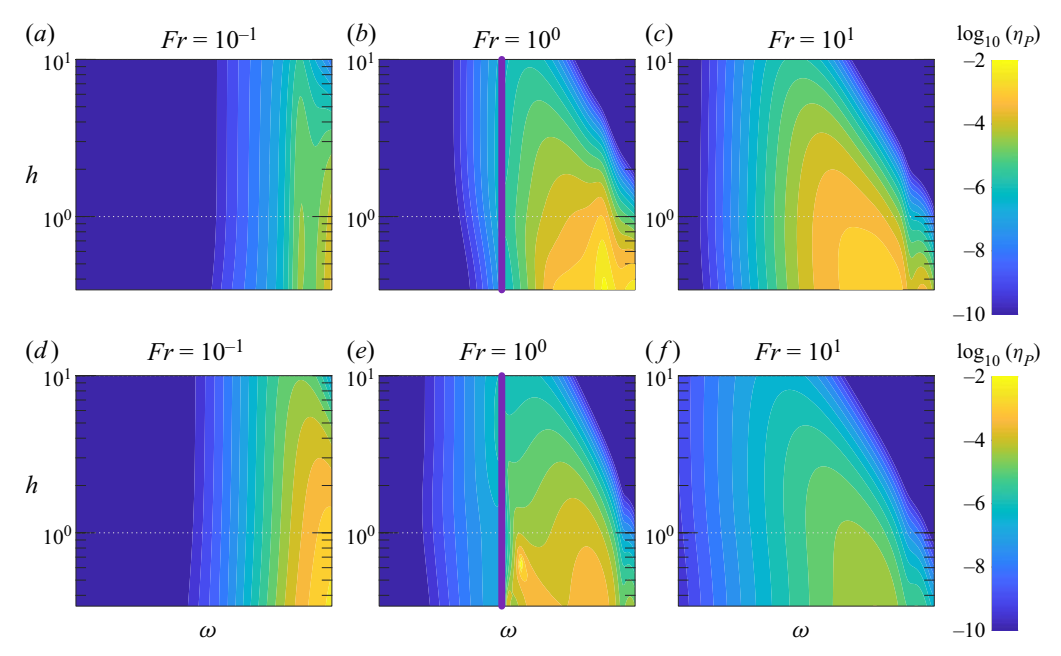


Figure 7. Similar to figure 6, except that it shows the contour of η_P .

frequency at low Fr flow conditions and, to a much less degree, is dependent on α (figures 8a-c). The central role of having larger α is to expand the energetic range to smaller ω while the energy level remains similar. The most energetic condition here is associated with stiffer plates and higher frequencies.

On the other hand, the electrical power output is highly dependent on α for higher Fr cases when the plate is in the supercritical condition (right of the purple line in figures 8d–f). Here, the power output increases rapidly with α , and attains its maximum values at $\alpha \approx 3$. However, the maximum energy output level is less than the value observed in the subcritical condition. The maximum deflection of the plate is almost independent of the α values, except for certain conditions of large α and stiff plates (figure 8a) where the large electromechanical coupling results in higher effective bending stiffness and reduction of the wave-induced vibration amplitude.

The effects of resistive and inductive properties of the plate, quantified with β and τ , are shown in figure 9 for different U^* values. In the following discussion, we focus specifically on Fr=0.1, h=1 and $\alpha=0.5$ to represent the energetic condition of figure 8. Two distinct ω values, 1 and 10, are tested, where it is found that the electric inductance can enhance the output power over a narrow range $\tau\omega\approx 1$. Over this range, there is a destabilizing effect from the inductance, and as a result, the plate flutters with a higher amplitude. This trend is intact across different U^* , suggesting that the inductive properties can merely be adjusted based on the wave frequency, independent of the plate flexibility, to reach a better energy harvester. The very large τ limit acts similarly to a short circuit and results in minimal effective coupling between electrical and mechanical fields. Consequently, the electric power output approaches zero regardless of β for $\tau\gg\omega$. On the other hand, there is no inductance destabilization effect in small $\tau\ll\omega$ regimes, and the electric circuit is purely resistive. In this case, the output power is just a function of β and reaches its maximum value when $\beta\omega\approx 1$.

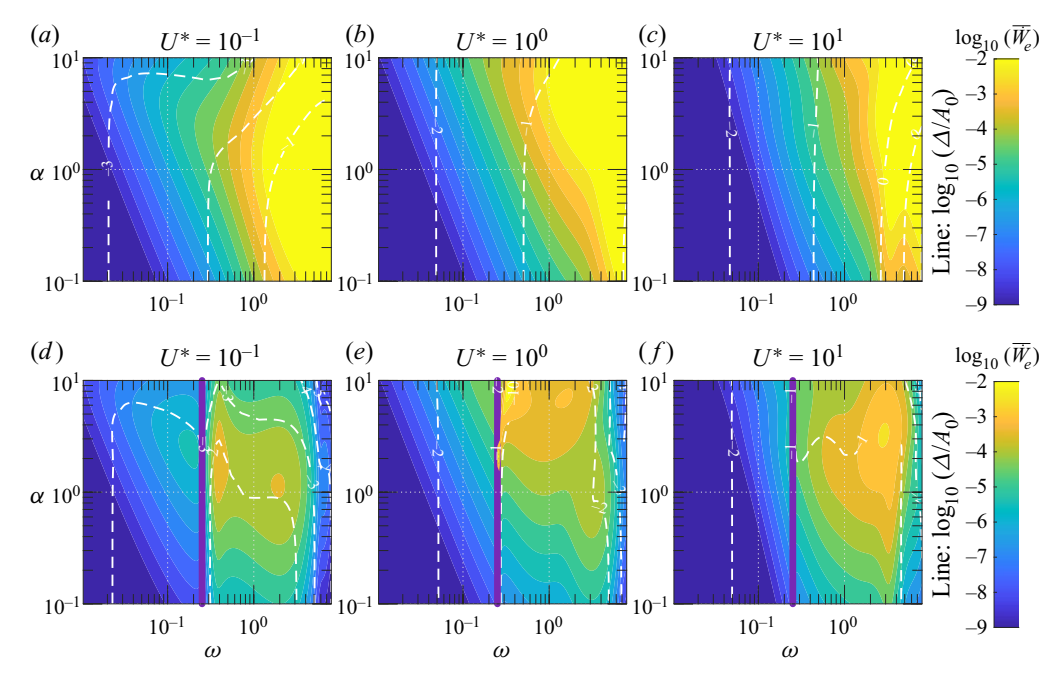


Figure 8. The effect of electromechanical coupling coefficient α on the average power output and plate's lateral deflection for three representative values $U^* = 0.1, 1, 10$ in (a-c) the subcritical condition with Fr = 0.1, and (d-e) the critical condition with Fr = 1. Here, h = 1.0, $\beta = 1$ and $\tau = 0$.

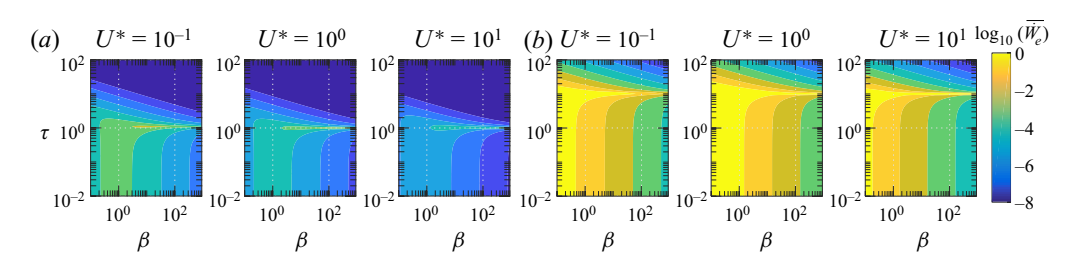


Figure 9. Dependency of the average electrical power output to inductive and resistive properties of the plate for (a) $\omega = 1$ and (b) $\omega = 10$. Here, $Fr = 10^{-1}$, h = 1.0 and $\alpha = 0.5$, selected based on results in figure 8.

5. Conclusion

This work explores the energy production from a two-dimensional electromechanical flexible plate placed in the proximity of a free surface and exposed to incident travelling gravity waves and incoming current. The model represents a range of multi-segmented hybrid current/wave energy harvesting devices. In order to capture the interaction between the body, wake, and incident, diffracted and radiated gravity waves, a Green's function of a moving vortex near the free surface in inviscid flow is utilized. Through this theoretical model, we identified the optimal conditions for energy production, and examined the predominant vibration modes of flexible plates situated near the free surface.

Two distinct conditions with maximum energy production levels are identified: one is associated with the cantilever fluttering mode of the plate, and the other is very similar to the flow-induced flapping motion of the plate. The study demonstrates that the optimal energy production regimes exhibit similar trends and are influenced by

changes in the Froude number. However, these energetic conditions occur at different non-dimensional flexibility values for the plate. The optimal flexibility for the cantilever fluttering mode remains relatively consistent across various incoming wave frequencies and Froude numbers. In contrast, the optimal flexibility for the flapping mode decreases progressively as the wave frequency increases. This divergent behaviour between the two modes provides valuable insights about selecting and adjusting the mechanical parameters of hybrid wave/current energy harvesting devices.

The vibration amplitude and electrical power output are highly dependent on the Froude number. In particular, their contour plots show a distinct behaviour in the subcritical, critical and supercritical flow conditions associated with Fr < 1, Fr = 1 and Fr > 1, respectively. Moreover, the resultant surface waves from the plate presence in the flow, based on the $\omega Fr^2 = \frac{1}{4}$ condition, determines the energy output level and efficiency of the piezoelectric plate. It is seen that the submergence depth should be smaller than the plate length to reach a good energy production level. The dependency on the submergence depth is more stringent for flow-induced vibration modes than the cantilever fluttering mode.

The role of electrical parameters is more regular and does not modify substantially the optimal energy-producing conditions. Nonetheless, a larger electromechanical coupling coefficient modifies the dynamic characteristic of the system, especially more flexible plates vibrating in their flow-induced flapping mode. It mainly broadens the frequency range corresponding to near-maximum energy production behaviour. The optimal resistive value of the electric network related to wave frequency $\beta\omega\approx 1$ and the optimal electric inductance is associated with near resonance condition in the electric network, namely when $\tau\omega\approx 1$.

The results provided in this paper could be helpful in the estimation of the operating threshold of hybrid wave/current energy harvesting devices that resemble a piezoelectric plate. It can also be employed to adjust the system's parameters, in particular the length of the device, to reach one of the highest energy-producing conditions. The current theoretical prediction using the inviscid flow theory and linear approximation should be tested with future experiments and fully nonlinear fluid–structure interaction simulations (Vahab, Sussman & Shoele 2021). In addition, the proposed model and the dispersion relation are insufficient to explore the energy production of the system at the critical condition $\omega Fr^2 = \frac{1}{4}$, where a group of reflected and radiated waves combines into one wave with a zero group velocity and no ability to transport wave energy. It would be an interesting extension of this study to explore theoretically energy production under this condition.

The predictions from the current linear model suggest that with current piezoelectric materials, the energy efficiency of the device is less than 5%, much smaller than other conventional hydrokinetic energy harvesters (Drew, Plummer & Sahinkaya 2009). It is observed that with better-engineered electromechanical converters, and larger α coefficient and with the use of the inductive elements in the electrical conversion unit, the energy efficiency of the device can be much improved and becomes close to 40%. The flexible piezoelectric plates can also be employed as unsteady thrust-producing devices if they are attached to the side of a boat or ship and undergo combined plunge and pitch motions (Grue *et al.* 1988; Belibassakis & Politis 2013). In addition, these types of energy converters have a unique property that they can be deployed or collected easily depending on the sea condition. The current model can be employed to determine the performance of hybrid wave/current energy harvesters as both the thrust-generating and energy-producing devices in these conditions. The three-dimensional effects of finite-width plates could also

modify wave diffraction and energy production. Including the three-dimensional effects into the current framework is the subject of ongoing research.

Acknowledgements. The authors would like to acknowledge the Florida State University Research Computing Center and NSF ACCESS computational resources through grant no. CTS200043 on which these simulations were carried out.

Funding. This work is partially supported by NSF grant CBET-1943810.

Declaration of interests. The author reports no conflict of interest.

Author ORCIDs.

Kourosh Shoele https://orcid.org/0000-0003-2810-0065.

Author contributions. K.S. derived the theory, performed the analysis and wrote the paper.

Appendix A

In this appendix, we assume that all variables are dimensional and we derive the most general equation of the system, assuming inviscid irrotational two-dimensional flow with y=0 placed at the air–sea interface pointing upwards. The velocity u is expressed based on the gradient of a scalar potential Φ , as $u=\nabla\Phi$, and the conservation of mass requires that the potential satisfies Laplace's equation

$$\nabla^2 \Phi = 0. \tag{A1}$$

The pressure can be calculated from,

$$-\frac{P}{\rho} = gy + \frac{\partial \Phi}{\partial t} + \frac{1}{2} |\nabla \Phi|^2 + B(t), \tag{A2}$$

where B(t) is an arbitrary function of t that can be omitted by redefining Φ without affecting the velocity field.

We have two types of boundaries: the air—water interface, which is also called the free surface, and the wetted surface of an impenetrable solid, which in this study is the surface of a thin piezoelectric plate. Along both surfaces, the flow can have relative motion only in the tangential direction, and the instantaneous equation of boundary conditions can be written as

$$F(X(t), t) = y - \xi(x, t) = 0,$$
 (A3)

where ξ is the vertical coordinate measured from y = 0, and X(t) is a point on the interfaces moving with velocity U. By taking the derivative of (A3), and with the assumption of only tangential relative motion at the interfaces (equivalently $U \cdot \nabla F = u \cdot \nabla F$), we can write the condition of moving surfaces as

$$\frac{\partial \xi}{\partial t} + \frac{\partial \Phi}{\partial x} \frac{\partial \xi}{\partial x} = \frac{\partial \Phi}{\partial y}.$$
 (A4)

Equation (A4) defines the kinematic boundary conditions on the plate surface and also on the free surface. On both boundaries, it is necessary to add the dynamic boundary condition. On the free surface, with atmospheric pressure P_a , we can write

$$-\frac{P_a}{\rho} = g\eta + \frac{\partial \Phi}{\partial t} + \frac{1}{2} |\nabla \Phi|^2 \quad \text{on } y = \eta, \tag{A5}$$

where η is the surface wave height. This equation can be combined with (A4), and with the assumption of P_a = constant, we can write the dynamic condition on the free

surface as

$$\frac{\partial^2 \Phi}{\partial t^2} + g \frac{\partial \Phi}{\partial t} + \frac{\partial}{\partial t} u^2 + \frac{1}{2} u \cdot \nabla u^2 = 0 \quad \text{on } y = \eta.$$
 (A6)

With the presence of a current with velocity u_c along the x axis, we can use the superposition technique and define $\Phi = \Phi_w + u_c x$, where Φ_w is the velocity potential due to the surface waves, and $u_c x$ captures the effect of the current. To linearize the problem, we assume that certain physical scales of motion can be anticipated *a priori*, and define the non-dimensional quantities

$$\{\hat{x}, \hat{y}\} = \frac{2\pi\{x, y\}}{\lambda}, \quad \hat{t} = \omega t, \quad \hat{\eta} = \frac{\eta}{A}, \quad \hat{\Phi} = \frac{2\pi\Phi}{A\omega\lambda},$$
 (A7a-d)

where λ , ω and A are the typical values of wavelength, frequency and free-surface amplitude, respectively. We can rewrite (A1), (A3) and (A5) based on $\hat{\Phi}_w$ as

$$\nabla^2 \hat{\Phi}_w = 0, \tag{A8}$$

$$\frac{\partial \hat{\xi}}{\partial \hat{t}} + u_c \frac{\partial \hat{\eta}}{\partial \hat{x}} + \epsilon \left(\frac{\partial \hat{\Phi}_w}{\partial \hat{x}} \frac{\partial \hat{\eta}}{\partial \hat{x}} \right) = \frac{\partial \hat{\Phi}_w}{\partial \hat{y}} \quad \text{on } \hat{y} = \epsilon \hat{\eta}, \tag{A9}$$

$$\frac{\partial \hat{\Phi}_{w}}{\partial \hat{t}} + \left(\frac{2\pi g}{\omega^{2} \lambda}\right) \hat{\eta} + \frac{\epsilon}{2} \left(\hat{\nabla} \hat{\Phi}_{w}\right)^{2} = -\frac{2\pi P_{a}}{\rho A \omega^{2} \lambda} \quad \text{on } \hat{y} = \epsilon \hat{\eta}, \tag{A10}$$

where $\epsilon = 2\pi A/\lambda$ is the wave slope. If we assume $\epsilon \ll 1$, then we can drive the linear equations to $O(\epsilon)$, which in their non-dimensional forms based on u_c and b will be similar to (2.8), (2.9) and (2.10).

REFERENCES

ADERINTO, T. & LI, H. 2018 Ocean wave energy converters: status and challenges. *Energies* 11 (5), 1250. ALAM, M.-R. 2012 Nonlinear analysis of an actuated seafloor-mounted carpet for a high-performance wave energy extraction. *Proc. R. Soc.* A 468 (2146), 3153–3171.

ALBEN, S. 2008a The flapping-flag instability as a nonlinear eigenvalue problem. *Phys. Fluids* **20** (10), 104106. ALBEN, S. 2008b Optimal flexibility of a flapping appendage in an inviscid fluid. *J. Fluid Mech.* **614**, 355–380. BABARIT, A. 2017 *Ocean Wave Energy Conversion: Resource, Technologies and Performance.* Elsevier.

BABARIT, A., GENDRON, B., SINGH, J., MÉLIS, C. & JEAN, P. 2013 Hydro-elastic modelling of an electro-active wave energy converter. In *International Conference on Offshore Mechanics and Arctic Engineering*, vol. 55430, V009T12A033. American Society of Mechanical Engineers.

BELIBASSAKIS, K.A. & POLITIS, G.K. 2013 Hydrodynamic performance of flapping wings for augmenting ship propulsion in waves. *Ocean Engng* 72, 227–240.

COLLINS, I., HOSSAIN, M., DETTMER, W. & MASTERS, I. 2021 Flexible membrane structures for wave energy harvesting: a review of the developments, materials and computational modelling approaches. *Renew. Sustain. Energy Rev.* **151**, 111478.

CRIMI, P. & STATLER, I.H. 1964 Forces and moments on an oscillating hydrofoil. In Fourth Symposium Naval Hydrodynamics, Office of Naval Research (ed. B.L. Silverstein), ACR-92, pp. 477–494. Office of Naval Research.

DOARÉ, O. & MICHELIN, S. 2011 Piezoelectric coupling in energy-harvesting fluttering flexible plates: linear stability analysis and conversion efficiency. J. Fluids Struct. 27 (8), 1357–1375.

DREW, B., PLUMMER, A.R. & SAHINKAYA, M.N. 2009 A review of wave energy converter technology. In Proceedings of the Institution of Mechanical Engineers, Part A: Journal of Power and Energy. 223 (8), 887–902.

ERTURK, A. & INMAN, D.J. 2011 Piezoelectric Energy Harvesting. John Wiley & Sons.

FALNES, J. & KURNIAWAN, A. 2020 Ocean Waves and Oscillating Systems: Linear Interactions Including Wave-Energy Extraction, vol. 8. Cambridge University Press.

- FISH, F.E. & ROHR, J.J. 1999 Review of dolphin hydrodynamics and swimming performance. *Space Nav. Warf. Syst. Cent. Tech. Rep.* 1801.
- GRUE, J., MO, A. & PALM, E. 1988 Propulsion of a foil moving in water waves. *J. Fluid Mech.* 186, 393–417.
 GRUE, J. & PALM, E. 1985 Wave radiation and wave diffraction from a submerged body in a uniform current. *J. Fluid Mech.* 151, 257–278.
- HASKIND, M.D. 1954 On wave motion of a heavy fluid. Prikl. Mat. Mekh. 18, 15-26.
- JBAILY, A. & YEUNG, R.W. 2015 Piezoelectric devices for ocean energy: a brief survey. *J. Ocean Engng Mar. Energy* 1 (1), 101–118.
- KOOLA, P.M. & IBRAGIMOV, A. 2003 The dynamics of wave carpet a novel deep water wave energy design. In Oceans 2003. Celebrating the Past... Teaming Toward the Future (IEEE Cat. No. 03CH37492), vol. 4, pp. 2288–2293. IEEE.
- MICHELE, S., BURIANI, F., RENZI, E., VAN ROOIJ, M., JAYAWARDHANA, B. & VAKIS, A.I. 2020 Wave energy extraction by flexible floaters. *Energies* 13 (23), 6167.
- MICHELE, S., ZHENG, S. & GREAVES, D. 2022 Wave energy extraction from a floating flexible circular plate. *Ocean Engng* 245, 110275.
- MICHELIN, S. & DOARÉ, O. 2013 Energy harvesting efficiency of piezoelectric flags in axial flows. J. Fluid Mech. 714, 489–504.
- MOUGEL, J. & MICHELIN, S. 2020 Flutter and resonances of a flag near a free surface. *J. Fluids Struct.* **96**, 103046.
- MUTSUDA, H., TANAKA, Y., DOI, Y. & MORIYAMA, Y. 2019 Application of a flexible device coating with piezoelectric paint for harvesting wave energy. *Ocean Engng* 172, 170–182.
- MUTSUDA, H., WATANABE, R., AZUMA, S., TANAKA, Y. & DOI, Y. 2013 Ocean power generator using flexible piezoelectric device. In *International Conference on Offshore Mechanics and Arctic Engineering*, vol. 55423, V008T09A002. American Society of Mechanical Engineers.
- NEWMAN, J.N. 2018 Marine Hydrodynamics. The MIT Press.
- NITSCHE, M. & KRASNY, R. 1994 A numerical study of vortex ring formation at the edge of a circular tube. J. Fluid Mech. 276, 139–161.
- PALM, E. & GRUE, J. 1999 On the wave field due to a moving body performing oscillations in the vicinity of the critical frequency. *J. Engng Maths* **35** (1), 219–232.
- PECHER, A. & KOFOED, J.P. 2017 Handbook of Ocean Wave Energy. Springer Nature.
- PENG, H.H., QIU, W., MENG, W., CHEN, M., LUNDRIGAN, B. & GARDINER, T. 2020 Experimental studies and time-domain simulation of a hinged-type wave energy converter in regular waves. *Mar. Syst. Ocean Technol.* **15** (1), 1–15.
- PULLIN, D.I. & WANG, Z.J. 2004 Unsteady forces on an accelerating plate and application to hovering insect flight. J. Fluid Mech. 509, 1–21.
- REECE, J.W. 1963 Motion of a flexible hydrofoil near a free surface. PhD thesis, University of Florida.
- REECE, J.W. & SIEKMANN, J. 1964 Swimming of a flexible hydrofoil near a free surface. Z. Angew. Math. Mech. 44 (12), 559–571.
- RENZI, E. 2016 Hydroelectromechanical modelling of a piezoelectric wave energy converter. *Proc. R. Soc.* A 472 (2195), 20160715.
- RENZI, E., MICHELE, S., ZHENG, S., JIN, S. & GREAVES, D. 2021 Niche applications and flexible devices for wave energy conversion: a review. *Energies* 14 (20), 6537.
- RINGWOOD, J.V. 2020 Wave energy control: status and perspectives 2020. IFAC-PapersOnLine 53 (2), 12271–12282.
- ROZHDESTVENSKY, K.V. & RYZHOV, V.A. 2003 Aerohydrodynamics of flapping-wing propulsors. *Prog. Aerosp. Sci.* **39** (8), 585–633.
- SAFFMAN, P.G. 1995 Vortex Dynamics. Cambridge University Press.
- SELVAN, S.A. & BEHERA, H. 2020 Wave energy dissipation by a floating circular flexible porous membrane in single and two-layer fluids. *Ocean Engng* **206**, 107374.
- SHOELE, K. & MITTAL, R. 2016 Energy harvesting by flow-induced flutter in a simple model of an inverted piezoelectric flag. *J. Fluid Mech.* **790**, 582–606.
- SHOELE, K. & ZHU, Q. 2015 Drafting mechanisms between a dolphin mother and calf. *J. Theor. Biol.* 382, 363–377.
- STANSBY, P., MORENO, E.C. & STALLARD, T. 2015 Capture width of the three-float multi-mode multi-resonance broadband wave energy line absorber M4 from laboratory studies with irregular waves of different spectral shape and directional spread. *J. Ocean Engng Mar. Energy* 1 (3), 287–298.
- TAN, H.S. 1955 On source and vortex of fluctuating strength travelling beneath a free surface. *Q. Appl. Maths* 13 (3), 314–317.

K. Shoele

- TAN, H.S. 1957 Waves produced by a pulsating source travelling beneath a free surface. *Q. Appl. Maths* **15** (3), 249–255.
- THOMAS, O., DEÜ, J.-F. & DUCARNE, J. 2009 Vibrations of an elastic structure with shunted piezoelectric patches: efficient finite element formulation and electromechanical coupling coefficients. *Intl J. Numer. Meth. Engng* 80 (2), 235–268.
- THWAITES, B. & MEYER, R.E. 1960 Incompressible aerodynamics. J. Appl. Mech. 27 (4), 760.
- VAHAB, M., SUSSMAN, M. & SHOELE, K. 2021 Fluid-structure interaction of thin flexible bodies in multi-material multi-phase systems. *J. Comput. Phys.* 429, 110008.
- VIET, N.V., Wu, N. & WANG, Q. 2017 A review on energy harvesting from ocean waves by piezoelectric technology. *J. Model. Mech. Mater.* 1 (2), 20160161.
- XIA, Y., MICHELIN, S. & DOARÉ, O. 2015 Fluid-solid-electric lock-in of energy-harvesting piezoelectric flags. Phys. Rev. Appl. 3 (1), 014009.
- ZHENG, S., MEYLAN, M.H., FAN, L., GREAVES, D. & IGLESIAS, G. 2020 Wave scattering by a floating porous elastic plate of arbitrary shape: a semi-analytical study. *J. Fluids Struct.* **92**, 102827.
- ZHENG, S., MEYLAN, M., ZHANG, X., IGLESIAS, G. & GREAVES, D. 2021 Performance of a plate-wave energy converter integrated in a floating breakwater. *IET Renew. Power Gen.* 15 (14), 3206–3219.
- ZHU, Q., LIU, Y. & YUE, D.K.P. 2006 Dynamics of a three-dimensional oscillating foil near the free surface. *AIAA J.* 44 (12), 2997–3009.
- ZHU, Q. & PENG, Z. 2009 Mode coupling and flow energy harvesting by a flapping foil. *Phys. Fluids* **21** (3), 033601.